ARTICLE

Title Passive multistage solar desalination enables durable high-efficiency freshwater production

Received 00th January 20xx,
Accepted 00th January 20xx

DOI: 10.1039/x0xx00000x

Wenzong Li[a], Tianyi Ma[b], Xu Wang[a], Lemin Zhang[a], Wenna Ge[a], Chenguang Lu[a], Xiangge Bai[a], Jiahui Chu[a], Zichao Yuan[a], Shile Feng[a] and Yahua Liu [a, c]

1. Supplementary Note：

Supplementary Note S1. Heat transfer efficiency test on the SMVAs and aluminum sheet

To ensure consistent surface emissivity between the SMVAs and the aluminum substrate, both surfaces were uniformly coated with a thin layer of black multi-walled carbon nanotubes (MWCNTs). An infrared camera was employed to monitor the surface temperature increase under one sun illumination (Fig. S7a). The temperature distributions of SMVAs and the aluminum sheet are presented in Fig. S7b. As shown in Fig. S7c, SMVAs exhibits a higher heating rate and equilibrium temperature under one sun illumination compared to the aluminum sheet. This phenomenon is attributed to the V-groove structure, which enlarges the heat dissipation area and enhances heat concentration on the surface.

Supplementary Note S2. Water evaporation rate test on the SMVAs

To evaluate the evaporation performance of SMVAs, we investigated the evaporation behavior of the water film on its surface under one sun illumination (Fig. S8a–b). When the surface temperature of the SMVAs reaches a steady state, 100 mg of water is deposited on the test surface. SMVAs The 100 mg of water was evaporated completely within 350 s (Fig. S8a, orange curve; Fig. S8b). Notably, the calculated evaporation rate at 30-second intervals remained consistently around 0.3 mg s^{-1} (Fig. S8a, blue points), further confirming that the high thermal conductivity of SMVAs effectively promotes water evaporation on its surface.

Supplementary Note S3. Photothermal performance of different solar absorbers

An aqueous dispersion of TiN and MCNT was prepared at a mass ratio of 1:20. The resulting mixture was uniformly coated onto the surface of SMVAs using spin coating, followed by natural drying at ambient temperature to form a photothermal coating. Fig. S10a shows a scanning electron microscopy (SEM) image of the MCNT coating, revealing a highly uniform and smooth surface. In contrast, the MCNT-TiN photothermal coating which consists of massive mountain-shaped microscale structures. Energy-dispersive spectroscopy (EDS) analysis confirmed the presence of nitrogen (N), titanium (Ti), and carbon (C) within these structures (Fig. S10b), which proved the mountain-like microstructure arises from the aggregation of MCNT and TiN.

According to the light-trapping principle, the microstructures on the surface of the MCNT-TiN coating can reduce solar reflectance, thereby enhancing solar energy utilization. The absorption spectrum in Fig. S 10c demonstrates broadband ultrahigh light absorption of up to 96.5% for the MCNT-TiN coating across the entire measured wavelength range, significantly exceeding that of other coatings. Consequently, the MCNT-TiN coating demonstrates a superior heating rate and a higher equilibrium temperature under one-sun illumination compared to other coatings. The temperature of the MCNT-TiN coating increases from 23 °C to 73.5 °C within 200 s (Fig. S11a). Remarkably, despite the presence of numerous mountain-like microstructures on the surface of the MCNT-TiN coating, the temperature distribution remains exceptionally uniform (Fig. S11b).

Supplementary Note S4. Solar-steam conversion efficiency of SMVAs-C

The solar-steam conversion efficiency η is expressed as

$$\eta = m h_v / C_{opt} P_o \quad (1)$$

where m represents the net evaporation rate of SMVAs-C (1.31 kg m^{-2} h^{-1}), h_v refers to the equivalent evaporation enthalpy of water (2350 J g^{-1}). C_{opt} refers to the optical concentration on evaporator surface. P_o is the solar irradiation power of one sun (1 kW m^{-2}). Therefore, the solar-steam conversion efficiency is approximately 83% under one sun illumination.

[a] State Key Laboratory of High-performance Precision Manufacturing, Dalian University of Technology, Dalian 116024, P. R. China.
[b] Library, Dalian University of Technology, Dalian 116024, P. R. China.
[c] Department of Anaesthesiology, Central Hospital of Dalian University of Technology, Dalian 116033, P. R. China.
†Supplementary Information available: [details of any supplementary information available should be included here]. See DOI: 10.1039/x0xx00000x

Supplementary Note S5. Flow rate on the SMVAs

Under dark conditions, the flow rate on the SMVAs is approximately 2.1 $cm^3\ h^{-1}$. Under one sun illumination, the flow rate on the SMVAs decreases to approximately 1.25 $cm^3\ h^{-1}$ (Fig. S14a). The energy loss to the bulk water is calculated by the equation

$$Q_1=CmΔT \quad (2)$$

where Q_1 referred to the heat energy transfer from the evaporator to bulk water by conduction, C was the specific heat capacity of pure water (4.2 kJ $kg^{-1}\ K^{-1}$), m was the mass of concentrated brine discharged from the surface of SMVAs. and $ΔT$ is the temperature change of concentrated brine under one sun irradiation. Therefore, the conduction heat loss of the evaporator was ~3% under one sun irradiation. As a result, the temperature of the SMVAs with a higher flow rate is nearly identical to that of the static surface (Fig. S14b).

Note S6. Energy loss analysis of SMVAs-C

The energy loss during the entire process can be attributed to four main factors: one-dimensional steady-state heat transfer, conduction, radiation, convection, and reflection. Each heat loss parameters were calculated as follows:

(1) One-dimensional steady-state heat transfer

$$Q=\frac{t_1-t_2}{\frac{\delta_1}{\lambda_1}+\frac{\delta_2}{\lambda_2}} \quad (3)$$

where Q referred to the heat energy transfer from the evaporator top to air by one-dimensional steady-state heat transfer, t_1 was the temperature of photothermal coating, t_2 was the temperature of PMMA surface, δ_1 was the thickness of air layer (10 mm), δ_2 was the thickness of PMMA (0.5 mm), λ_1 was coefficient of thermal conductivity of air (0.025 W $m^{-1}\ K^{-1}$) and λ_2 was coefficient of thermal conductivity of PMMA (0.2 W $m^{-1}\ K^{-1}$). Therefore, the heat loss due to conduction from the evaporator to the surrounding air is approximately 0.9% under one sun irradiation.

(2) Radiation

$$Q_r=\varepsilon A\sigma(T_s^4-T_0^4) \quad (4)$$

where ε corresponding to the emissivity (assumed to be 1), A was the evaporator area, and σ was the Stefan-Boltzmann constant (5.669×10^{-8} W $m^{-2}\ K^{-4}$), T_s was associated to the temperature of evaporator surface, T_0 was the ambient water temperature. The surface radiation heat loss accounts for ~2.5% of the total received energy.

(3) Convection

$$Q_c=hA(T_s-T_0) \quad (5)$$

where h was the convection heat transfer coefficient (5 W $m^{-2}\ K^{-1}$). The convection heat loss made up for 7.25% of the total received energy.

(4) Reflection

The measured average reflection loss of photothermal coating over the broad solar spectrum (200-2500 nm) was ~3.35%. Therefore, the sum of calculated energy losses is 15% under one sun irradiation.

Note S7. Thermal conductivity measurements of SMVAs

The thermal conductivity of the SMVAs was measured using a Netzsch laser flash apparatus (LFA 467), which employs a non-contact transient method to determine thermal diffusivity (α). The thermal conductivity, k (W $m^{-1}\ K^{-1}$), was calculated according to

$$k=\alpha\rho C_p \quad (6)$$

where α ($mm^2\ s^{-1}$) is the measured thermal diffusivity, ρ (g cm^{-3}) is the density, and C_p (J $g^{-1}\ K^{-1}$) is the specific heat capacity. The heat capacity C_p was measured by differential scanning calorimetry (DSC Q20). The parameters used to calculate the thermal conductivity of the SMVAs are summarized in Table R1.

Table S1. Thermal conductivity calculation parameters of SMVAs

Temperature (K)	α ($mm^2\ s^{-1}$)	ρ (g cm^{-3})	C_p (J $g^{-1}\ K^{-1}$)
293	70.251	4	0.8
303	71.319	4	0.81
313	70.426	4	0.83
323	69.548	4	0.84
333	69.079	4	0.86

The thermal conductivity of the SMVAs in the temperature range of 293–333 K was calculated using Eqs. (6) and the parameters listed in Table S1, with the results shown in Fig. 16b. The SMVAs exhibit a high thermal conductivity of up to 220 W $m^{-1}\ K^{-1}$.

Note S8. Mechanism of high evaporation performance of MPSDA

In a multistage system, the latent heat of condensation released in one stage is reused for evaporation in subsequent stages. As a result, vapor production increases across multiple evaporators, improving overall system efficiency (Fig. S21a). The efficiency of a multistage system can be expressed[1] as

$$\eta=\frac{\sum_1^n q_n}{q_{in}} \quad (7)$$

where q_{in} is the input heat flux and q_n is the heat flux from vaporization at the n^{th} stage as

$$q_n=h_v m_n \quad (8)$$

Here, h_v is the vaporization enthalpy and m_n is the vapor mass flux, which can be calculated by Fick's law of diffusion [2] as

$$m_n=-D_a\frac{d\rho}{dx}\approx D_a\frac{\rho_e-\rho_c}{b} \quad (9)$$

where D_α is the mass diffusivity, and ρ_e and ρ_c are the saturated vapor concentration at the evaporator and the condenser,

respectively, determined by their interface temperatures. The vapor concentration is given by the Antoine equation as

$$\rho = \frac{P}{RT} \quad (10)$$

where R is the universal gas constant [3], and T represents the temperature of evaporation interface (T_e) and the temperature of condensation interface (T_c). The saturated vapor pressure P is expressed as

$$log_{10} P = A - \frac{B}{C+T} \quad (11)$$

where A, B, and C [3,4] are component specific constants. The diffusion coefficient D_a is

$$D_a = D_0 \left(\frac{T_n}{T_0}\right)^{\frac{3}{2}} \quad (12)$$

with $T_n=(T_{e\text{-}n}+T_{c\text{-}n+1})/2$ as the mean stage temperature and D_0 the coefficient evaluated at the reference temperature T_0 = 298.15 K.

For simplicity, we assumed $T_{e\text{-}n}=T_{c\text{-}n}$ because the evaporator and condenser are thin (0.5 mm) and in thermal contact. As shown Fig. S21b, we measured steady-state temperatures using thermocouples. Evaporation rates for systems with varying stage numbers were then calculated iteratively from Eqs. (9)–(12), showing good agreement with experimental results (Fig. S21c). Substituting these evaporation masses into Eqs. (7)–(8) yielded energy utilization efficiencies consistent with experiments (Fig. S21d).

Note S9. Evaporation performance of MPSDA on cloudy weather.

To further evaluate device performance under different weather conditions, we conducted an outdoor test on a cloudy day (Fig. S23a). The setup was installed on the rooftop of School of Mechanical Engineering, Dalian University of Technology, and experiments were carried out on August 28, 2025, from 8:00 am to 4:00 pm. A total of 27 mL of water was collected over 8 hours (Fig. s23b), corresponding to an average productivity of 670 mL kW^{-1} h^{-1}. Although cloudy conditions and solar flux fluctuations reduced overall performance, the multi-stage evaporator still exhibited strong outdoor productivity.

Notes and references

1 L. Zhang, Z. Xu, B. Bhatia, B. Li, L. Zhao and E. N. Wang, *Applied Energy*, 2020, **266**, 114864

2 Z. Xu, L. Zhang, L. Zhao, B. Li, B. Bhatia, C. Wang, K. L. Wilke, Y. Song, O. Labban, J. H. Lienhard, R. Wang and E. N. Wang, *Energy Environ. Sci.*, 2020, **13**, 830-839.

3 B. E. Poling, J. M. Prausnitz, O. C. John Paul and R. C. Reid, The properties of gases and liquids, Mcgraw-hill New York, 2001.

4 E. Chiavazzo, M. Morciano, F. Viglino, M. Fasano and P. Asinari, *Nat. Sustain.*, 2018, **1**, 763-772

2. Supplementary Figures:

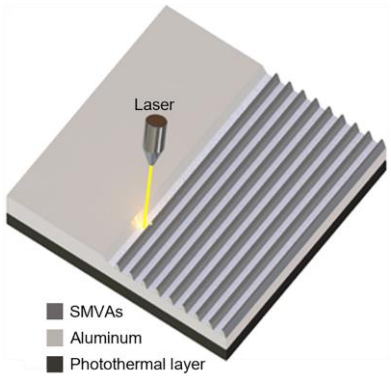

Fig. S1 Schematic showing the fabrication process of SMVAs.

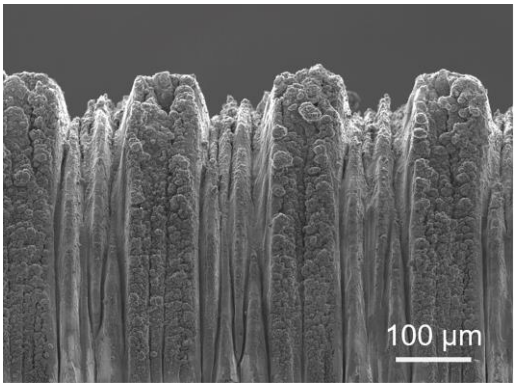

Fig. S2 Cross sectional SEM image of SMVAs

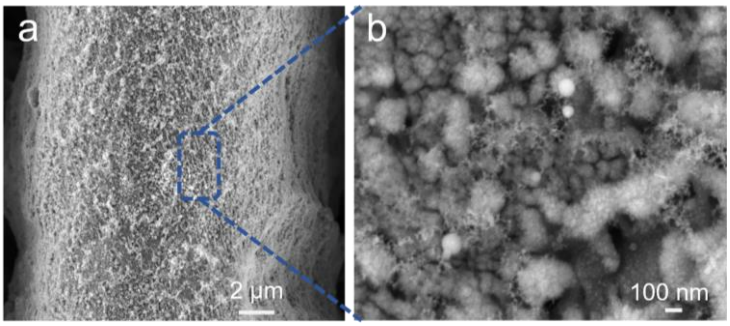

Fig. S3 High-magnification SEM image of the microslot on the SMVAs.

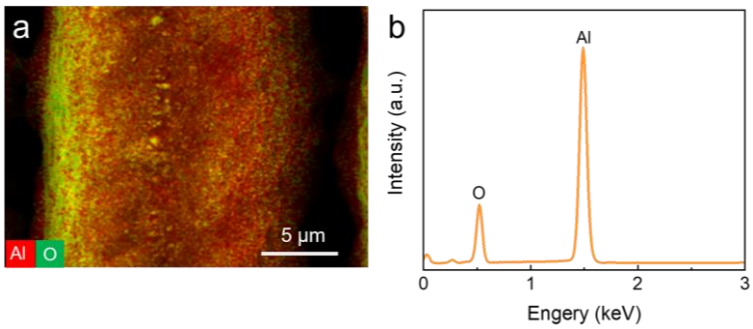

Fig. S4 Energy-dispersive spectroscopy (EDS) analysis. (a) Elemental distribution of aluminum and oxygen on the microslot surface; (b) Overall distribution map of aluminum and oxygen elements.

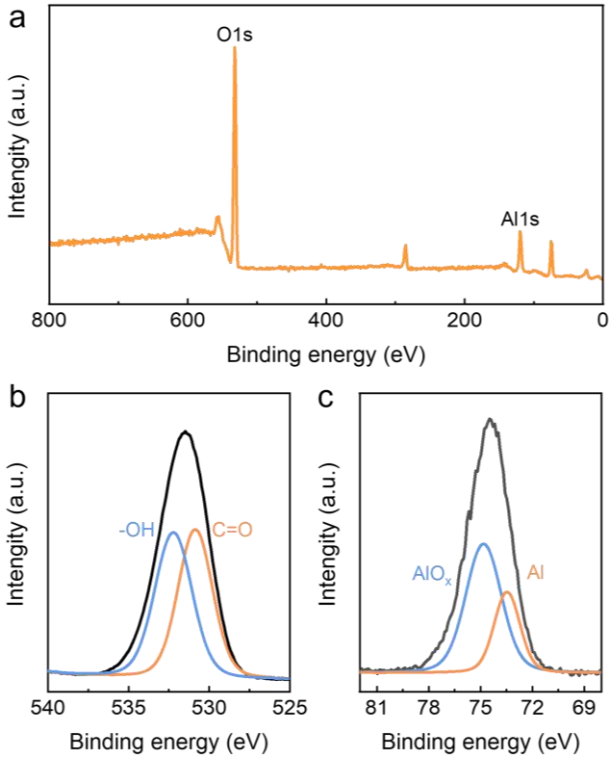

Fig. S5 (a)The XPS spectra of SMVAs. (b) High-resolution XPS spectra of O1s regions of SMVAs. (c) High-resolution XPS spectra of Al1s regions of SMVAs.

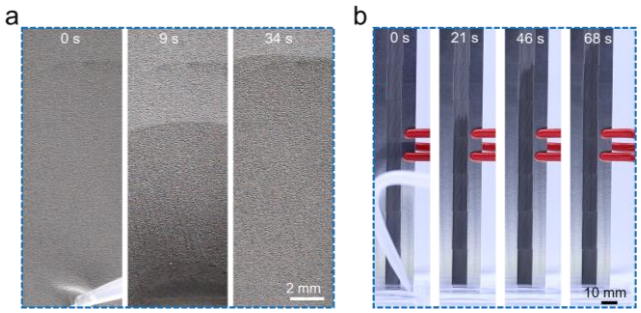

Fig. S6 (a) Sequential images showing the wicking behavior of a water droplet on the SAS. (b) Sequential images illustrating the maximum water transport distance on the SMVAs.

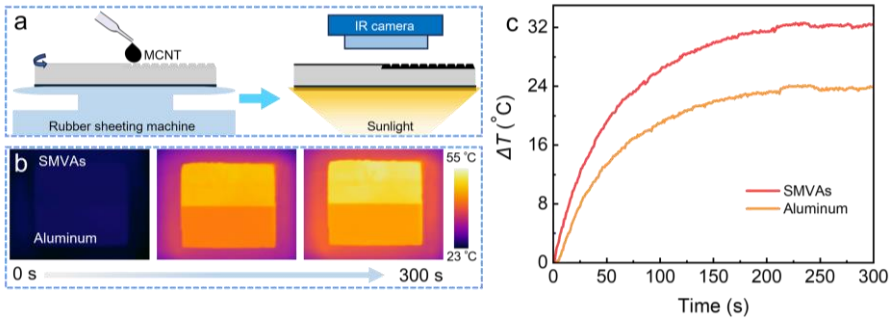

Fig. S7 Heat transfer efficiency of the SMVAs and aluminum sheet. (a) Schematic showing the experimental setup for evaluating the heat transfer performance of SMVAs and an aluminum sheet. (b) Infrared thermal images of the SMVAs and an aluminum sheet under 1-sun irradiation. (c) Temperature variation over time on the SMVAs and an aluminum sheet.

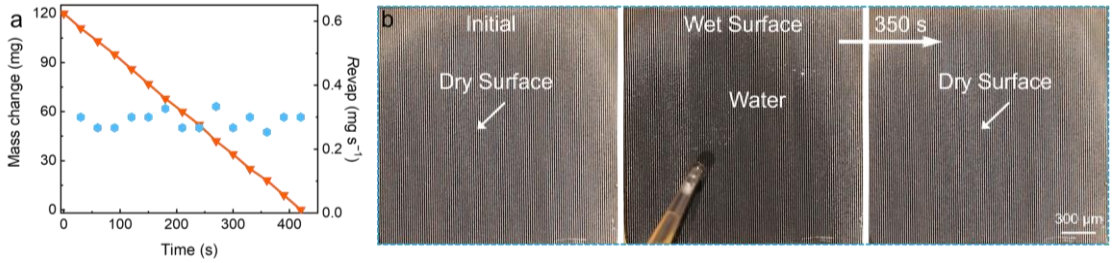

Fig. S8 Water evaporation rate on the SMVAs. (a) Mass change of a 100 μL water droplet over time on the SMVAs under 1-sun solar illumination (orange curve) and corresponding evaporation rate (blue dots). (b) Sequential images of water evaporation on the SMVAs.

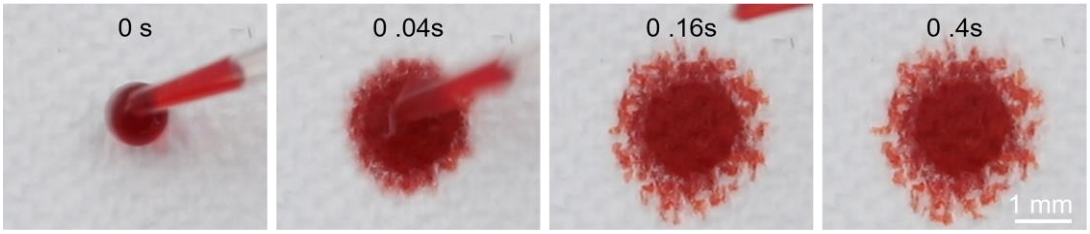

Fig. S9 Image sequences of the wicking behavior of a water droplet on the superhydrophilic glass fiber.

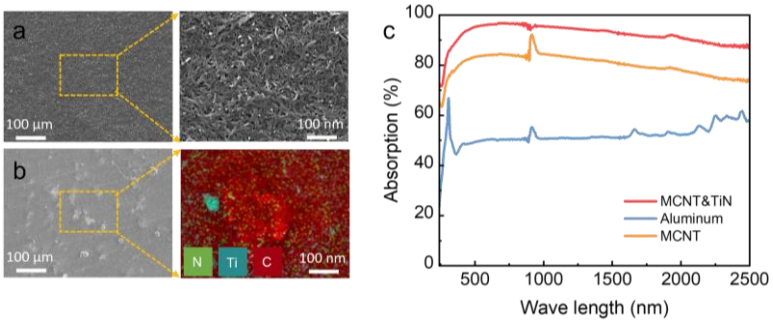

Fig. S10 Characterization of different photothermal coatings. (a) Surface morphology of the MCNT coating. (b) Surface morphology of the MCNT&TiN coating and corresponding elemental distribution of nitrogen (N), titanium (Ti), and carbon (C). (c) Absorption spectra of different coatings in the wavelength range of 200–2500 nm.

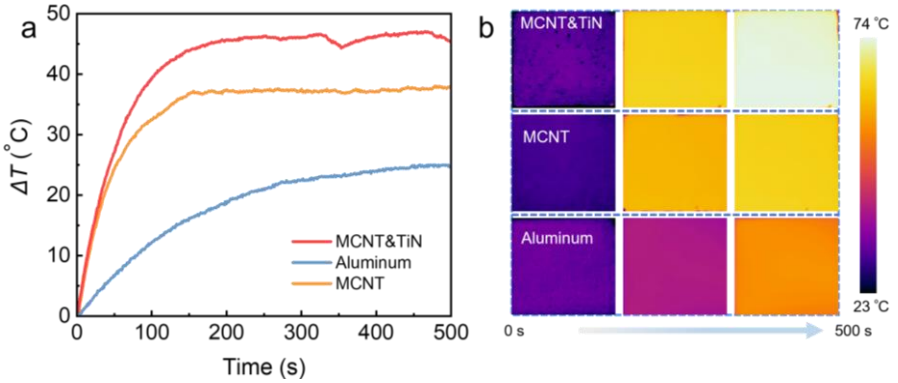

Fig. S11 Photothermal performance of different photothermal coatings. (a) Temperature variation over time for different photothermal coatings. (b) Temperature distribution of different photothermal coatings captured by an infrared (IR) camera.

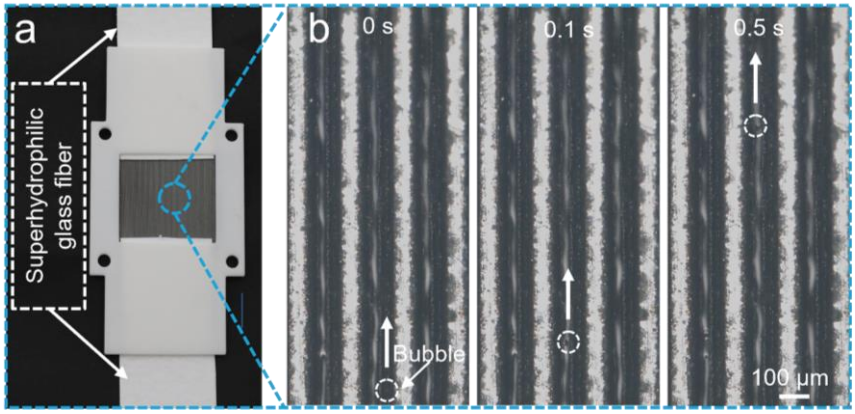

Fig. S12 (a) Photograph of the SMVAs-C evaporator. (b) Sequential images depicting the continuous, rapid water flow on the surface of SMVAs-C. The water on the SMVAs exhibits laminar flow, with the rapid movement of bubbles providing indirect evidence of the flow dynamics.

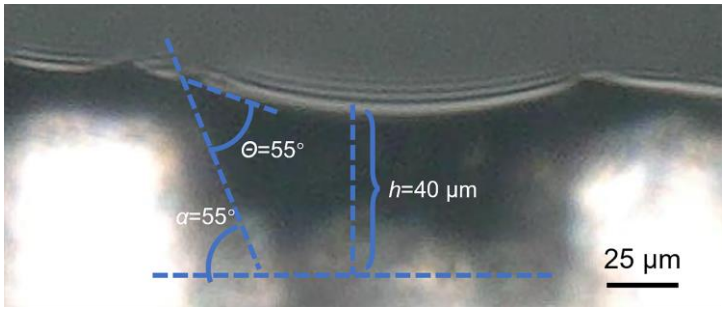

Fig. S13 Groove angle (α) of SMVAS, the liquid–surface contact angle (θ) and liquid surface thickness (h).

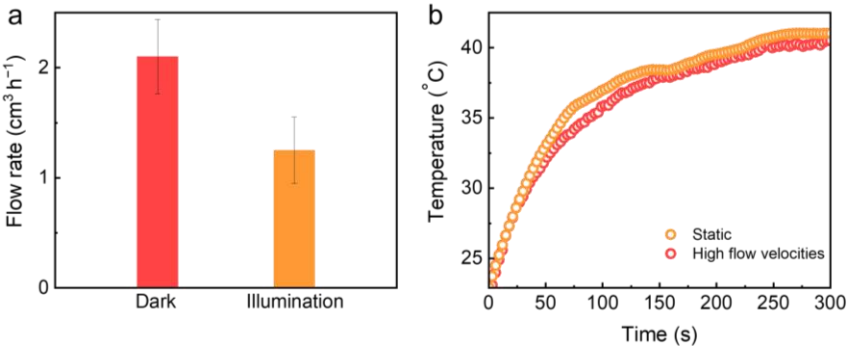

Fig. S14 (a) Flow rate on the SMVAs. (b) Temperature variation over time for surfaces with different flow velocities.

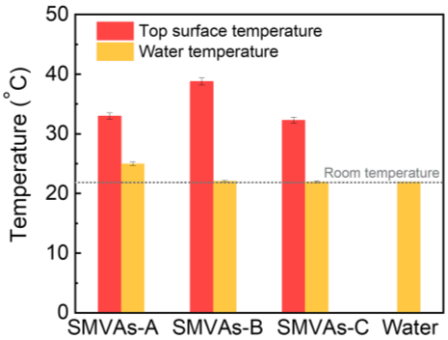

Fig. S15 Temperature gradient of different types evaporators under one sun illumination.

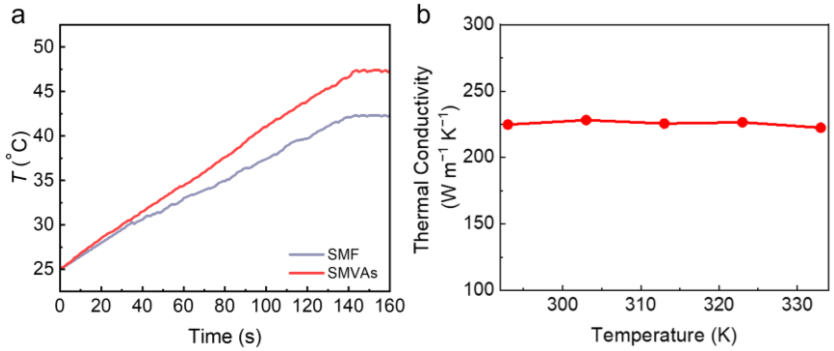

Fig. S16 (a)Temperature variation over time for surfaces with different thermal conductivity. (b) The thermal conductivity of the SMVAs.

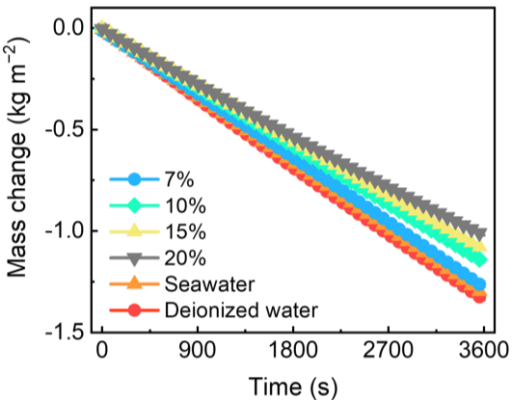

Fig. S17 Water mass variation of the SMVAs-C evaporator using feedwater with different salinities.

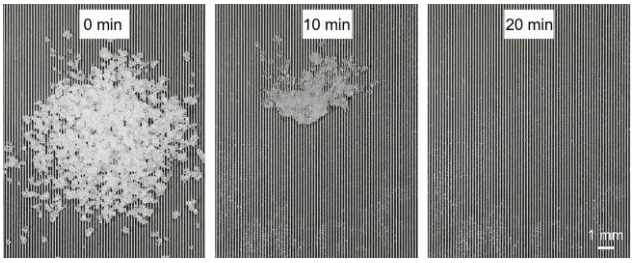

Fig. S18 Time-lapse optical images illustrating the rejection process of a 20 mg NaCl solid crystal from the SMVAs into the bulk water over 20 minutes.

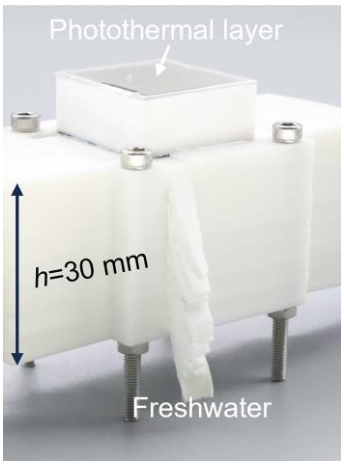

Fig. S19 Photograph of the indoor experimental setup.

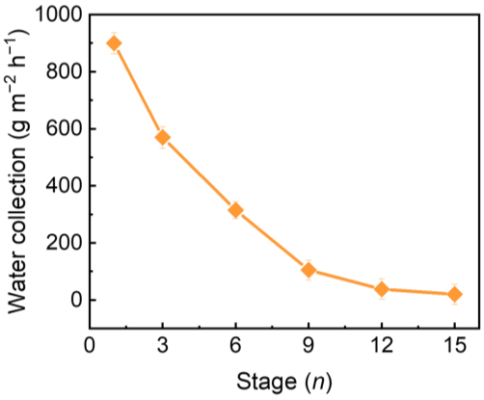

Fig. S20 Water collection rates at different stages of MPSDA.

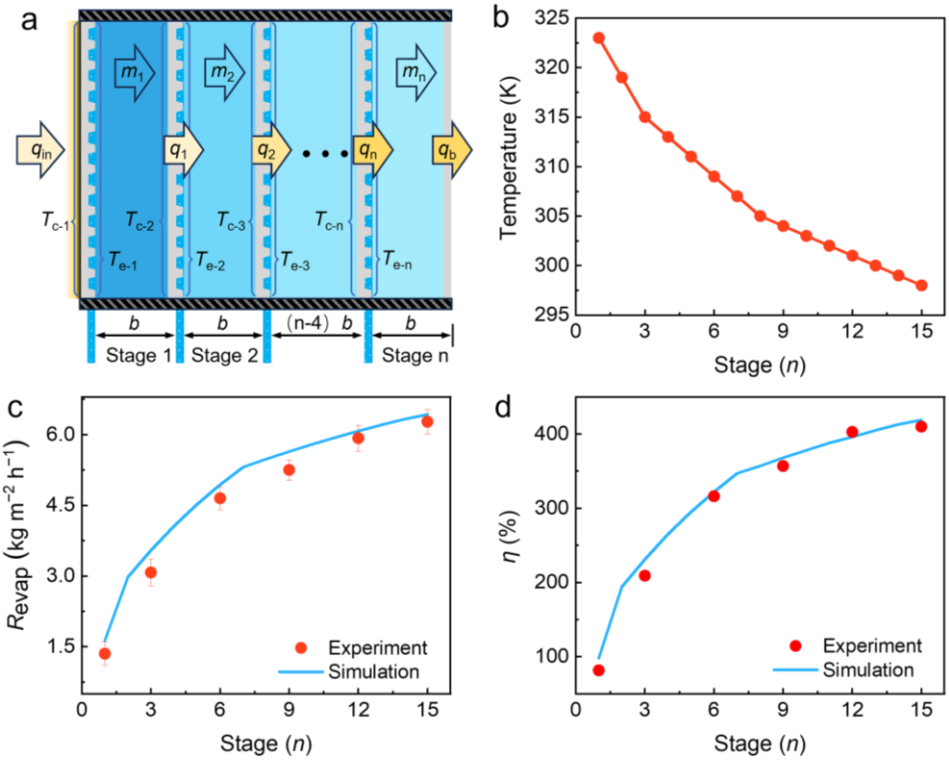

Fig. S21 Mechanism underlying high evaporation performance. (a) Schematic of mass transfer in the multi-stage evaporator. (b) Steady-state temperature of each stage. (c) Steady-state vapor mass flux of each stage. (d) Steady-state energy utilization efficiency of each stage.

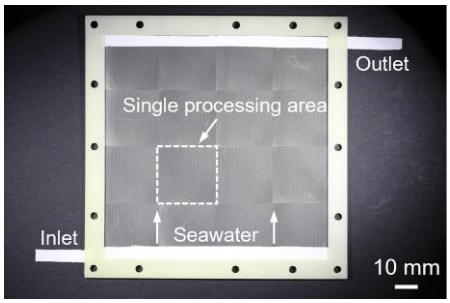

Fig. S22 Photograph of the water inlet and outlet of the outdoor experimental device.

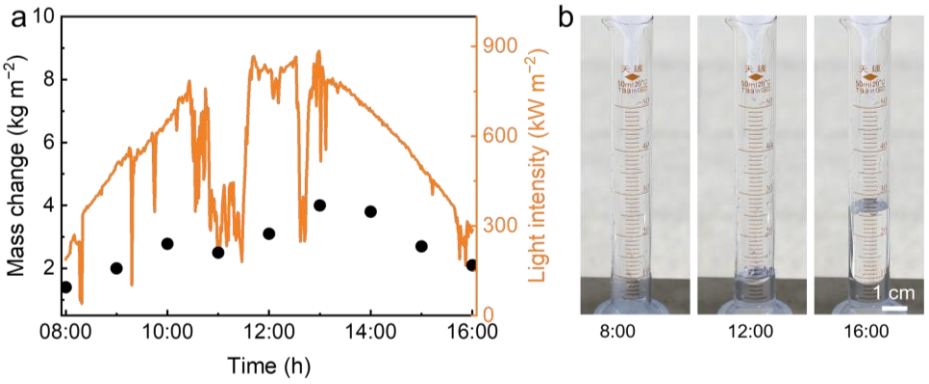

Fig. S23 (a) Temporal variations of evaporation rate and solar flux. (b) Time-lapse optical images of water collected in a graduated cylinder.

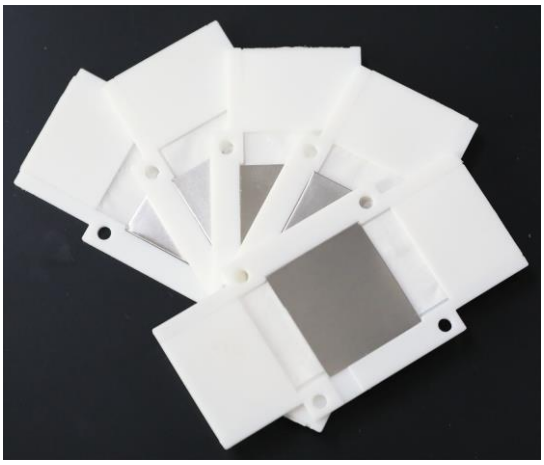

Fig. S24 Optical image of individual stages of the multi-stage evaporator.

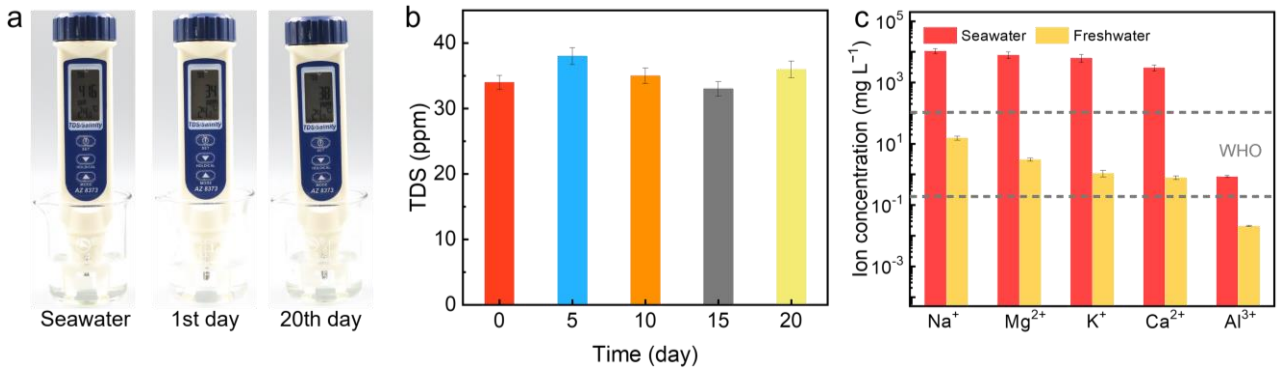

Fig. S25 Water quality monitoring of the MPSDA. (a)-(b) TDS levels during 20 days of continuous operation. (c) Ion concentration during 20 days continuous of operation.

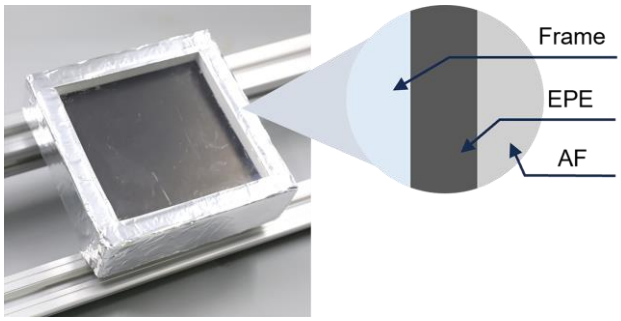

Fig. S26 Photograph of the protective case.

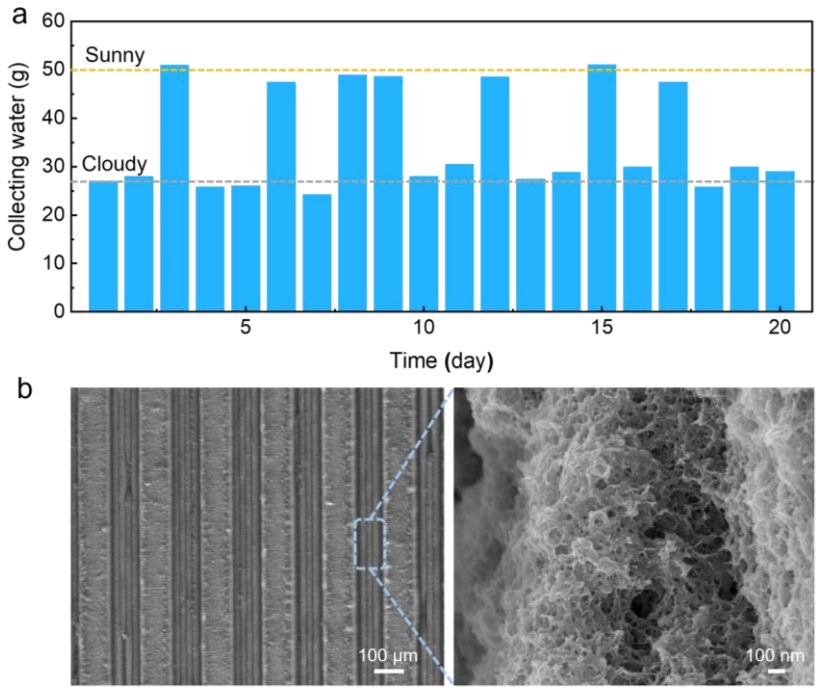

Fig. S27 Evaporation stability of multi-stage evaporator. (a) Freshwater collection quality of the MPSDA during 20 days of continuous operation. (b) SEM images of the SMVAs V-groove structure after 20 days of continuous operation.